

Dynamic Load Model for Data Centers with Pattern-Consistent Calibration

Siyu Lu, *Student Member, IEEE*, Chenhan Xiao, *Student Member, IEEE*, and Yang Weng, *Senior Member, IEEE*

Abstract—The rapid growth of data centers has made large electronic load (LEL) modeling increasingly important for power system analysis. Such loads are characterized by fast workload-driven variability and protection-driven disconnection and reconnection behavior that are not captured by conventional load models. Existing data center load modeling includes physics-based approaches, which provide interpretable structure for grid simulation, and data-driven approaches, which capture empirical workload variability from data. However, physics-based models are typically uncalibrated to facility-level operation, while trajectory alignment in data-driven methods often leads to overfitting and unrealistic dynamic behavior. To resolve these limitations, we design the framework to leverage both physics-based structure and data-driven adaptability. The physics-based structure is parameterized to enable data-driven pattern-consistent calibration from real operational data, supporting facility-level grid planning. We further show that trajectory-level alignment is limited for inherently stochastic data center loads. Therefore, we design the calibration to align temporal and statistical patterns using temporal contrastive learning (TCL). This calibration is performed locally at the facility, and only calibrated parameters are shared with utilities, preserving data privacy. The proposed load model is calibrated by real-world operational load data from the MIT Supercloud, ASU Sol, Blue Waters, and ASHRAE datasets. Then it is integrated into the ANDES platform and evaluated on the IEEE 39-bus, NPCC 140-bus, and WECC 179-bus systems. We simulate the dynamic responses of heterogeneous LELs, including data centers, cryptocurrency mining facilities, and hydrogen electrolyzers, under system-level disturbances. We find that interactions among LELs can fundamentally alter post-disturbance recovery behavior, producing compound disconnection-reconnection dynamics and delayed stabilization that are not captured by uncalibrated load models.

Index Terms—Data centers, Dynamic Load Modeling, Pattern-Consistent Calibration, Transient Stability Analysis

I. INTRODUCTION

The rapid growth of large-scale data centers has introduced a new class of grid-side demand, operating at tens to hundreds of megawatts and exhibiting fast variability and protection-driven disconnection behavior [1]. Data centers may abruptly disconnect from the grid to safeguard critical server equipment during voltage or frequency disturbances [2]. Such disconnections can shed large volumes of load, creating power imbalances that lead to further voltage and frequency deviations in the grid. These deviations will compromise generator synchronism and degrade power quality, increasing the risk of regional stability events, including cascading outages [3], [4]. Recent events include a 1,500 MW simultaneous data center load loss in 2024 [5], which caused a frequency and voltage rise to 60.047 Hz and 1.07 p.u. These events demonstrate that such system-level risks are both practical and urgent. In response to

these emerging risks, such loads have been formally defined as large electronic loads (LELs), constituting a distinct class of load demand for focused study [3]. As data centers continue to scale and cluster geographically [6], dynamic load modeling of data centers and their grid-side behavior has become essential for reliable power system planning and operation [7], [8].

Prior to the expansion of data centers, conventional large-load modeling primarily focused on industrial facilities such as factories and steel mills [9]. These loads were typically represented using continuous electromechanical dynamics formulated as ordinary differential equations [10], often combined with static ZIP components to capture steady-state voltage-power characteristics [11]–[13]. Despite their effectiveness in modeling slowly varying electromechanical loads, these models are limited for modern LELs, such as data centers. Unlike traditional industrial facilities, data centers interface with the grid primarily through power-electronic conversion stages, and are driven by rapidly-changing and often stochastic computational loads [1].

To address this issue, recent load modeling approaches developed for data centers can be broadly classified into data-driven and physics-based methods [14]. Data-driven methods learn load behavior directly from historical measurements, using statistical models such as Hidden Markov Models [15], and learning-based models [16] such as recurrent neural network [17]. While these methods can closely fit training data, their lack of explicit physical structure prevents generalization at a structural level, which makes them unreliable under unseen operating conditions for simulation-based load modeling and grid-side behavior analysis. To resolve this issue, physics-based load modeling approaches explicitly represent the major subsystems of data centers, including IT workloads, cooling systems, and protection mechanisms, using physically motivated formulations [18]–[22]. For example, IT workload dynamics have been modeled using Poisson processes to capture stochastic computational job arrivals [18]. These physically interpretable models capture data center load behavior at a structural level, reflecting dominant operating regimes that shape characteristic patterns of load behavior. However, compared to data-driven approaches, they generally lack the flexibility to adapt load model parameters to the facility-specific operating patterns. This limits their effectiveness in realistic grid simulations, where heterogeneous data center facilities exhibit distinct load patterns that require facility-specific parameter calibration.

Given these limitations, a natural direction is to develop a data center load modeling framework that not only retains a physics-based backbone but also incorporates a calibrated, data-driven capability to align temporal and statistical load patterns when adapting model parameters to individual fa-

cilities. To this end, this paper formulates data center load modeling as a parameterized protocol, explicitly designed to support subsequent calibration using operational data. Building on recent advances that decompose data center load into IT workload, cooling load, auxiliary load, and protection mechanism [18], [22], each subsystem is parameterized according to its underlying physical structure and the characteristic load patterns it induces. Specifically, IT workload is represented using a duty-idle operating pattern, with server utilization modeled as an Ornstein-Uhlenbeck process [23]. Cooling and auxiliary subsystems are modeled using established motor-based dynamic equations and ZIP representations [24]. Disconnection and reconnection behaviors are captured through a rule-based parameterization that reflects protection logic and operational constraints [25].

Building on this physics-based backbone, we propose a data-driven calibration approach tailored to data center load characteristics for robust parameter estimation with alignment of temporal and statistical load patterns. Since the data center load is inherently stochastic, directly aligning with instantaneous load can easily lead to overfitting. A more practical strategy is to align the temporal and statistical features of the load, which is sufficient for system operators to reproduce realistic load behavior [1]. To extract such features, we adopt temporal contrastive learning (TCL) [26], as it provides an unsupervised, window-based representation that discriminates between distinct operating regimes while capturing invariant temporal patterns. This approach follows directly from the characteristics of data center loads. It exhibits recurring burst-idle windows driven by job scheduling [1], requiring discrimination among operating regimes and invariance to nuisance variations including small timing shifts and amplitude scaling. Calibration is then performed by aligning TCL-based feature representations extracted from real facility-level load and simulated load trajectories.

Additional benefits of our design include generalization from data centers to other LELs, as well as privacy-preserving deployment for data center operators. These properties arise directly from the parameterized modeling and decentralized calibration architecture, which are designed to abstract shared structural load behaviors while avoiding the exchange of raw operational data. Beyond data centers, the parameterized modeling extends to other emerging LEL types, like cryptocurrency mining facility [27], [28] and hydrogen electrolyzers [29], [30]. They share common structures, including duty-idle workload dynamics, cooling and auxiliary load patterns, and protection-driven disconnection behavior. By abstracting these shared structures, the unified parameterization improves the efficiency of large-scale grid simulations involving heterogeneous LELs. The calibration pipeline is shown in Fig. 1. The utility first distributes an uncalibrated load model to LEL facilities. Each facility then performs pattern-consistent calibration locally and returns only calibrated model parameters. Throughout this process, raw operational load, particularly workload traces, are never shared. It preserves data privacy and prevents disclosure of proprietary operational information related to computing utilization and business strategies [31], [32].

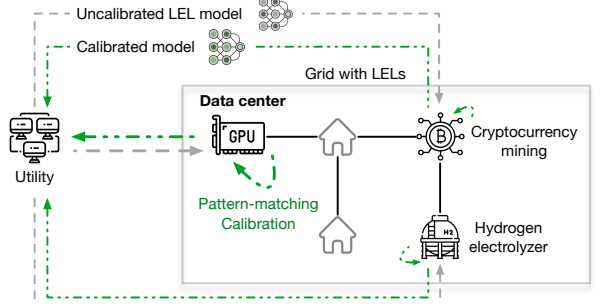


Fig. 1. Pattern-consistent calibration framework for realistic LEL dynamic behavior in grid analysis with data privacy preserved.

To evaluate dynamic responses under system-level disturbances, we design validation studies to capture variations in network scale, geographical grid characteristics, and heterogeneous LEL deployment. Accordingly, simulations are conducted on IEEE 39-bus, NPCC 140-bus, and WECC 179-bus systems using ANDES [33]. To enhance realism, model parameters are calibrated using operational data from both academic and industrial computing facilities, including MIT Supercloud [34], ASU Sol, Blue Waters [35], and ASHRAE [36], with protection and reconnection parameters derived from utility reports [8]. The results demonstrate that parameter calibration is critical for accurately capturing the system-level impacts of LELs in dynamic grid simulations.

The remainder of the paper is organized as follows. Section II presents the physics-based, parameterized load modeling backbone. Section III introduces the pattern-consistent calibration framework. Section IV evaluates mixed-LEL simulations using ANDES. Section V concludes the paper.

II. PARAMETERIZED PHYSICS-BASED LOAD MODELING OF DATA CENTERS

To enable efficient calibration under heterogeneous and facility-specific operational data, we propose a physics-based load modeling backbone with explicit parameterization. It enables calibration by tuning a small set of physically meaningful parameters, rather than learning unconstrained input-output mappings as in pure data-driven load modeling [15]–[17]. Following established data center modeling practices [18]–[22], the aggregate load is decomposed into IT workload (Section II-A), cooling load and auxiliary load (Section II-B). A parameterized protection mechanism is further introduced to describe disconnection and reconnection behavior (Section II-C). Together, these components capture the essential dynamics of data center power consumption.

A. Duty-Idle Workload Modeling

In data centers, IT workload power consumption dominates the total electrical demand, typically accounting for more than half of total demand [37]. Accordingly, IT workload is treated as the core subsystem in the proposed load model. Within IT workloads, CPU and GPU utilization can rapidly transition between idle and peak duty in response to computational job arrivals, as observed in MIT Supercloud GPU utilization traces [34]. Accordingly, a duty-idle formulation [18] is adopted for workload modeling following:

$$p_{\text{work}}(t) = p_{\text{base}} + \eta(t) (p_{\text{full}} - p_{\text{base}}), \quad \eta(t) \in [0, 1], \quad (1)$$

where p_{base} denotes the standby or idle power draw, p_{full} is the rated full-duty power, and $\eta(t)$ denotes the instantaneous utilization level. In Eq. (1), accurately modeling $\eta(t)$ is central to capturing workload bursts, sustained high-utilization periods, and return-to-idle behavior in data centers.

In prior work, $\eta(t)$ has often been modeled using Poisson-based processes to capture stochastic computational job arrivals [18]. However, Poisson processes are memoryless and therefore produce unrealistically abrupt fluctuations (see bottom panel of Fig. 2). When used in isolation, they cannot capture the temporal correlation observed in real CPU/GPU workloads. Moreover, data center loads typically exhibit mean reversion around nominal utilization levels. To capture these characteristics while preserving stochasticity, we introduce temporal coupling and mean-reverting dynamics into the Poisson-based workload model. This formulation naturally leads to an Ornstein–Uhlenbeck (OU) process [23]:

$$\tau_\eta \dot{\eta} = -(\eta - \mu_\eta) + \xi(t) + \sum_k A_k \delta(t - t_k), \quad (2)$$

where $\tau_\eta > 0$ is the time constant governing mean reversion, $\mu_\eta \in [0, 1]$ is the nominal utilization level, and $\xi(t)$ is a zero-mean stochastic perturbation with variance σ_ξ^2 capturing continuous workload fluctuations. The impulse term represents burst events, where event times t_k follow a Poisson process with rate λ and amplitudes A_k are drawn from a log-normal distribution with parameters θ_A . The resulting workload dynamics combine mean reversion, continuous stochastic variation, and burst events, producing trajectories that are both smooth and bursty (see the top panel of Fig. 2), directly reflecting the dominant temporal characteristics observed in real CPU/GPU utilization data (see Section IV-B).

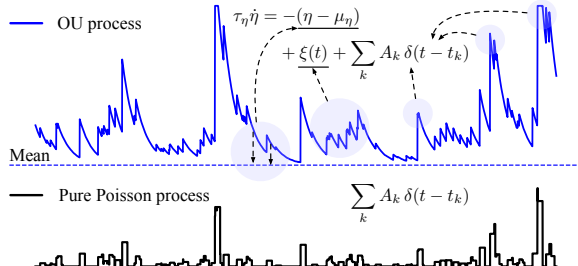


Fig. 2. Illustration of an OU process in Eq. (2) and a Poisson process. The pure Poisson process is memoryless and too stochastic.

Although this subsection focuses on data center workloads, similar duty-idle patterns arise in other LELs. For example, in cryptocurrency mining facilities, the duty state corresponds to active hashing operation, while the idle state reflects curtailed or suspended mining [27], [28]. In hydrogen electrolyzers, the duty state corresponds to active electrolysis [30], while reduced or zero production represents an idle state. These similarities allow the OU-based workload module to be reused across LEL types to enable unified parameterization.

To support the pattern-consistent calibration framework introduced in Section III, the key workload parameters are

$$\Theta_{\text{work}} = \{p_{\text{base}}, p_{\text{full}}, \tau_\eta, \mu_\eta, \sigma_\xi, \lambda, \theta_A\}. \quad (3)$$

B. Cooling and Auxiliary Load Modeling

Beyond IT workload-driven consumption, cooling systems account for the majority of the remaining power demand [37] for LELs. Since cooling units (e.g., chillers, compressors, fans, and pumps) are predominantly motor-driven, the aggregated cooling load can be represented using the Western Electricity Coordinating Council (WECC) Composite Load Model for Dynamic Simulations (CMPLDW) framework [38]. Within this framework, the dynamic behavior of the cooling motors is modeled in the synchronous rotating direct-quadrature reference frame (dq -frame), and the instantaneous active and reactive power consumption is computed as

$$\begin{aligned} p_{\text{cool}}(t) &= v_{ds}(t) i_{ds}(t) + v_{qs}(t) i_{qs}(t), \\ q_{\text{cool}}(t) &= v_{qs}(t) i_{ds}(t) - v_{ds}(t) i_{qs}(t), \end{aligned} \quad (4)$$

where the stator voltages (v_{ds}, v_{qs}) are obtained from the terminal bus voltage, and the stator currents (i_{ds}, i_{qs}) arise from solving the coupled differential-algebraic equations governing stator and rotor fluxes, slip, and electromagnetic torque. These equations follow the standard WECC composite load motor formulation, parameterized by the electrical constants (R_s, X_s, X_m, R_r, X_r) and the mechanical inertia H_m [38].

Furthermore, cooling motors exhibit voltage-sensitive behavior during disturbances. Under deep voltage sags, reduced electromagnetic torque and increased reactive current demand accelerate rotor slip. Stalling occurs if $|V| < V_{\text{stall}}$ persists longer than τ_{stall} . When stalling is triggered, the cooling block remains disconnected for a recovery interval T_{cool} . To support the pattern-consistent calibration framework, we parameterize the cooling module by

$$\Theta_{\text{cool}} = \{R_s, X_s, X_m, R_r, X_r, H_m, V_{\text{stall}}, \tau_{\text{stall}}, T_{\text{cool}}\}. \quad (5)$$

The remaining data center power consumption is attributed to non-IT auxiliary loads, including lighting, control units, security electronics, networking equipment, and other miscellaneous components [18]. Due to their fast electrical response and negligible internal dynamics compared to cooling motors, these loads are modeled using a standard ZIP formulation [24]:

$$\begin{aligned} p_{\text{aux}}(V) &= p_{\text{aux},0} \cdot (\alpha_Z (\frac{V}{V_0})^2 + \alpha_I (\frac{V}{V_0}) + \alpha_P), \\ q_{\text{aux}}(V) &= \beta_{\text{aux}} \cdot p_{\text{aux}}(V), \end{aligned} \quad (6)$$

where $p_{\text{aux},0}$ denotes the nominal auxiliary active power at the reference voltage V_0 , β_{aux} is a constant power factor, and the coefficients satisfy $\alpha_Z + \alpha_I + \alpha_P = 1$. To support facility-specific calibration, the auxiliary module is parameterized by

$$\Theta_{\text{aux}} = \{p_{\text{aux},0}, \alpha_Z, \alpha_I, \alpha_P, \beta_{\text{aux}}\}. \quad (7)$$

C. Grid-Interfacing Protection and Recovery Modeling

To accurately reflect the data center load response to grid-level disturbances, we incorporate a protection and recovery module. In practice, data centers deploy multi-stage uninterruptible power supply systems (UPS) [1], [2] to isolate IT loads from the grid and provide local supply. Such protection is activated when voltage or frequency deviations exceed prescribed tolerance thresholds:

$$|V - V_{\text{ref}}| > \Delta V \text{ or } |\omega - \omega_{\text{ref}}| > \Delta \omega, \quad (8)$$

where ΔV and $\Delta\omega$ define the allowable deviations from the nominal voltage V_{ref} and frequency ω_{ref} . When protection is activated, partial or complete load shedding occurs and is modeled as

$$\tilde{p}_{\text{load}}(t) = \kappa(t)p_{\text{load}}(t), \quad \tilde{q}_{\text{load}}(t) = \kappa(t)q_{\text{load}}(t), \quad (9)$$

where $p_{\text{load}} = p_{\text{work}} + p_{\text{cool}} + p_{\text{aux}}$ denotes the aggregate pre-protection power demand, and $q_{\text{load}} = q_{\text{cool}} + q_{\text{aux}}$ denotes the corresponding reactive demand since the IT workload is assumed to operate at near-unity power factor. The term $\kappa(t) \in [0, 1]$ represents a retained-load fraction that captures the combined impact of UPS isolation for IT loads and protection-induced disconnection of cooling and auxiliary components.

To prevent nuisance responses to shallow or short-lived disturbances, protection actions are initiated only if the violation in Eq. (8) persists for longer than a minimum duration $t_{\text{delay}}^{\text{trip}}$, after which load shedding is triggered according to the retained-load formulation in Eq. (9).

After load shedding is triggered, recovery-driven reconnection is governed by both electrical and operational constraints. Under electrical constraints, the bus voltage and system frequency must return to acceptable bounds, $|V - V_{\text{ref}}| \leq \Delta V$ and $|\omega - \omega_{\text{ref}}| \leq \Delta\omega$ and remain stable for a waiting interval $t_{\text{wait}}^{\text{recon}}$. Under operational constraints, a minimum reconnection delay $t_{\text{delay}}^{\text{recon}}$ must elapse following disconnection, representing requirements such as UPS recharge or controller reset time. Once these conditions are met, the retained-load fraction $\kappa(t)$, constrained by $\kappa_{\min} \leq \kappa(t) \leq \kappa_{\max}$, is gradually restored toward unity under a ramp-rate constraint $\dot{\kappa}(t) \leq r_{\kappa}$. The parameter r_{κ} denotes a site-dependent reconnection rate that prevents unrealistic step changes in demand and captures staged restoration behavior.

Other LELs also have grid-interfacing protection. For example, cryptocurrency mining facilities typically rely on power supply unit (PSU)-level protection and feeder relays [2], [27], [28], while hydrogen electrolyzers incorporate programmable logic controller (PLC)-supervised stack protection [29], [30]. Therefore, this module can also extend across varied LELs. To support the pattern-consistent calibration framework, we parameterize the protection and recovery module by

$$\Theta_{\text{prot}} = \{V_{\text{ref}}, \omega_{\text{ref}}, \Delta V, \Delta\omega, t_{\text{delay}}^{\text{trip}}, t_{\text{wait}}^{\text{recon}}, t_{\text{delay}}^{\text{recon}}, \kappa_{\min}, \kappa_{\max}, r_{\kappa}\}. \quad (10)$$

III. PATTERN-CONSISTENT CALIBRATION FRAMEWORK

With the physics-based load model established and key parameters identified, we develop a pattern-consistent calibration framework to adapt the model to facility-specific data. A key insight is that grid planning and dynamic studies require reproducing the statistical and temporal patterns of LEL behavior rather than exact power trajectories, which are unnecessary and often restricted by privacy constraints. Each LEL site in the grid receives an uncalibrated load model from the utility and performs local calibration of the parameter sets $(\Theta_{\text{work}}, \Theta_{\text{cool}}, \Theta_{\text{aux}}, \Theta_{\text{prot}})$ using on-site measurements. Only the calibrated parameters are transmitted back to the utility, as illustrated in Fig. 1, avoiding the exchange of raw load data.

A. Statistical Pattern-Consistent Calibration

For the workload, cooling, and auxiliary subsystems, we calibrate the parameter sets $(\Theta_{\text{work}}, \Theta_{\text{cool}}, \Theta_{\text{aux}})$ by maintaining consistency in representative statistical patterns between real operational loads and simulated load trajectories, rather than by directly aligning the time-series trajectory. This is because, data center loads are unlabeled and inherently stochastic. In such cases, point-wise trajectory alignment is prone to overfitting and can lead to unrealistic load behavior during load simulation. We formalize this limitation in Lemma 1 using a simplified workload model from (2).

Lemma 1 (Overfitting risk of trajectory alignment for data center workloads). *Consider the core impulse-driven component of a data center workload modeling in Eq. (2): $I(t) = \sum_k \delta(t - t_k)$ over a finite time horizon $[0, T]$, where $\{t_k\}$ are the job-arrival times of a homogeneous Poisson process with rate $\lambda^* > 0$. A single time-series sequence of the impulse $I(t)$ over $[0, T]$ does not uniquely identify the generating rate λ^* .*

Proof. Under any homogeneous Poisson process with rate $\lambda > 0$, the likelihood of observing a time-series sequence $I(t)$ over $[0, T]$ with job-arrival times $0 < t_1 < \dots < t_n < T$ is: $\mathbb{P}(N(T) = n) = e^{-\lambda T} (\lambda T)^n / n!$, which is strictly positive. Hence infinitely many values of λ are compatible with the same observed sequence, and the generating rate cannot be uniquely identified from a single training sequence of $I(t)$. \square

Lemma 1 indicates that trajectory-level alignment constrains only a single realization and is insufficient to recover the underlying data center workload dynamics, motivating the use of richer statistical features beyond the raw load trajectory. Moreover, data center loads exhibit strong temporal locality and regime-switching behavior [1], motivating a window-based representation that can distinguish among operating regimes (e.g., burst, idle, sustained) while remaining invariant to nuisance variations such as small timing shifts and amplitude scaling. To this end, we extract representative temporal patterns from $\{x(t)\}_{t=1}^T$ using temporal contrastive learning (TCL) [26], where $\{x(t)\}_{t=1}^T$ denote the time-series load signal associated with a given subsystem, comprising active and reactive power measurements when available. TCL provides an unsupervised, window-based representation that enforces similar embeddings for augmented views of the same operational trace while separating representations of distinct traces, naturally satisfying the above requirements.

In TCL, the operational data $\{x(t)\}_{t=1}^T$ is segmented into N overlapping windows $x^{(i)} = \{x(t)\}_{t=t_i}^{t_i+L-1}$, $i = 1 \dots N$, where $L = \lceil T/(2N) \rceil$ denotes the window length, and $t_i = 1 + (i-1)L$ is the starting index of the i -th window. For each window $x^{(i)}$, two stochastic augmentations $\tilde{x}_1^{(i)}$ and $\tilde{x}_2^{(i)}$ are generated via random amplitude scaling and additive noise.

The augmented views $(\tilde{x}_1^{(i)}, \tilde{x}_2^{(i)})$ of the same window form a positive pair, while augmented windows associated with different indices $(\tilde{x}_k^{(j)}, \tilde{x}_k^{(j)})$, $k \in \{1, 2\}$ form negative pairs. The objective is to obtain similar representations for positive pairs and distinct representations for negative pairs. To this

end, an encoder network ϕ_ψ with parameters ψ maps each augmented window to a representation $z_k^{(i)} \in \mathbb{R}^d$:

$$z_k^{(i)} = \phi_\psi(\tilde{x}_k^{(i)}), \quad i = 1 \dots N, \quad k \in \{1, 2\}. \quad (11)$$

This encoder is trained by minimizing the contrastive loss $\sum_{i=1}^N -\log \frac{\exp(\text{sim}(z_1^{(i)}, z_2^{(i)})/\tau)}{\sum_{j=1}^N \exp(\text{sim}(z_1^{(i)}, z_2^{(j)})/\tau)}$, where $\text{sim}(\cdot, \cdot)$ denotes cosine similarity and τ is a temperature parameter.

After training, the encoder is fixed and applied to all windows $x^{(i)}$, yielding a set of representations $\{z_i\}_{i=1}^N$ with $z_i \in \mathbb{R}^d$. Each z_i captures the representative temporal pattern of the i -th window. To aggregate window-level information into a description of the entire time-series load, low-order statistics of $\{z_i\}_{i=1}^N$ are sufficient. Specifically, we compute the first- and second-order elementwise moments of the window representations to form the statistical pattern vector

$$s = \left[\begin{array}{c} \frac{1}{N} \sum_{i=1}^N z_i \\ \frac{1}{N} \sum_{i=1}^N [z_i - (\frac{1}{N} \sum_{i=1}^N z_i)] \odot^2 \end{array} \right] \in \mathbb{R}^{2d}, \quad (12)$$

where $(\cdot) \odot^2$ indicates elementwise squaring across representation dimensions.

For a given subsystem (workload, cooling, and auxiliary), let $\{x_{\text{data}}(t)\}_{t=1}^T$ denote the real operational data and $\{x_{\text{model}}^\Theta(t)\}_{t=1}^T$ denote the simulated trajectory based on the uncalibrated parameter $\Theta \in \{\Theta_{\text{work}}, \Theta_{\text{cool}}, \Theta_{\text{aux}}\}$. The corresponding statistical pattern vectors s_{data} and $s_{\text{model}}(\Theta)$ are obtained using Eq. (12). The pattern-consistent calibration is then performed by minimizing

$$\Theta^* = \arg \min_{\Theta} \|s_{\text{data}} - s_{\text{model}}(\Theta)\|_2^2. \quad (13)$$

B. Rule-Based Specification of Protection Parameters

Calibration of protection-related parameters Θ_{prot} differs fundamentally from that of workload, cooling, and auxiliary subsystems. Protection-driven disconnection and recovery-driven reconnection events are triggered infrequently, and are often absent from routine operational data [4]. As a result, attempting to estimate protection parameters purely from data is unreliable and can lead to unstable or nonphysical calibration results. Instead, these parameters are specified directly from facility protection settings, which are explicitly defined in practice and reflect established operational constraints while avoiding dependence on rare-event observations.

We therefore adopt a rule-based calibration approach for the protection parameter set Θ_{prot} . Specifically, each LEL facility provides Θ_{prot}^* directly through a standardized disclosure form that specifies its voltage and frequency trip thresholds, enforced time delays, throttling and reconnection ramp rates, and reconnection limits. These parameters encode the facility's internal protection settings and operational constraints without exposing raw operational data.

The overall calibration workflow is illustrated in Fig. 3. The resulting calibrated parameter set $\{\Theta_{\text{work}}^*, \Theta_{\text{cool}}^*, \Theta_{\text{aux}}^*, \Theta_{\text{prot}}^*\}$ ensures that the load model reproduces the empirical statistical structure observed in real load data, which is essential for accurate grid simulations in practice. After calibration, system-level assessment of LEL impacts becomes feasible, as each

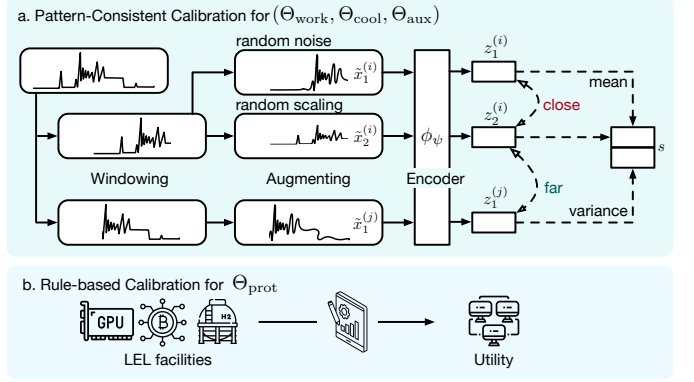


Fig. 3. Pattern-consistent calibration of LEL modeling parameters.

LEL site can independently obtain a calibrated load model. Section IV integrates multiple calibrated LEL instances into the ANDES [33] simulation platform to evaluate their collective effects on transient stability, disturbance propagation, and post-disturbance recovery behavior.

IV. NUMERICAL RESULTS

This section evaluates the proposed load modeling framework together with the pattern-consistent calibration approach, hereafter referred to as the calibrated LEL model. The evaluation is designed to assess whether calibrated load models reproduce realistic LEL behavior observed in real-world data, and how such behavior influences system-level responses under transient disturbances.

A. Experiment Setup

Evaluating the realism of calibrated LEL models using real-world workload traces from multiple large-scale computing facilities is a critical prerequisite for effective calibration. Specifically, workload data are drawn from the Massachusetts Institute of Technology (MIT) Supercloud dataset [34], the Arizona State University (ASU) Sol high-performance computing cluster, and the Blue Waters system monitoring dataset [35]. These datasets provide available CPU and GPU utilization measurements with associated power usage, covering diverse computing environments and operational regimes. For cooling and auxiliary subsystems, we adopt representative profiles reported by ASHRAE [36], as detailed cooling measurements are typically not shared by data center operators.

For each workload trace, the calibrated LEL model with pattern-consistent calibration is compared against representative baselines from both data-driven and physics-based modeling categories. For data-driven approaches, we consider a statistical Hidden Markov Model (HMM) [15] and a learning-based recurrent neural network (RNN) [17]. For physics-based modeling, we select a recent data center load model [18] as an uncalibrated baseline.

To study the interaction between LEL facilities and grid dynamics, transient simulations are conducted using ANDES [33], which supports customized differential-algebraic load subsystems and is well suited for large-scale transient stability analysis. Simulations are performed mainly on the IEEE 39-bus system, where a fixed number K of buses are randomly

selected and assigned as LEL sites. Each site is instantiated as one of three representative LEL representatives: data center, cryptocurrency mining facility, or hydrogen electrolyzer [2].

A three-phase fault is applied at a randomly selected bus at 5.0 s and cleared after 100 ms. To induce system dynamic responses. For reference, system responses obtained using the calibrated LEL model are compared against those produced by a conventional ZIP load model, representing traditional industrial loads such as steel mills, and the uncalibrated physics-based data center model [18]. Sensitivity analysis with respect to the LEL penetration level K is presented in Section IV-H, while scalability is examined in Section IV-G by extending the simulations to the NPCC 140-bus and WECC 179-bus benchmark systems.

Implementation details are as follows. Simulations are conducted using Python 3.12 and ANDES v1.9.3, with a fixed integration time step of $\Delta t = 1$ ms and a total simulation horizon of $T_{\text{sim}} = 40$ s. Differential-algebraic equations are solved using ANDES's implicit trapezoidal integration scheme with Newton-Raphson iterations at each time step. For the TCL feature module, we use a temporal window length of $L = 5$ and a feature dimension of $d = 64$.

B. Validation of Pattern-Consistent Calibration

We first validate the proposed pattern-consistent calibration framework by examining its ability to reproduce realistic workload, cooling, and auxiliary load dynamics observed in real-world data. For fair comparison, each load trace is split into disjoint training and testing segments. The data-driven baselines, HMM [15] and RNN [17], are trained on the training segment and evaluated using one-step-ahead prediction on the testing segment. The calibrated LEL model uses the same training data for parameter calibration and is then simulated forward over the testing period, while the uncalibrated physics-based baseline [18] is simulated on the testing segment using default parameters.

For workload validation, we use traces from the MIT Supercloud [34], the ASU Sol, and the Blue Waters dataset [35]. The results are shown in Fig. 4. The uncalibrated physics-based baseline produces overly oscillatory trajectories that fail to capture the temporal structure of empirical workloads across all three datasets, indicating unrealistic LEL behavior that can mislead grid-impact assessments. The data-driven baselines, HMM and RNN, reproduce some local patterns but tend to regress toward average behavior during the testing period. For example, although both models align with the workload trajectory during a relatively steady operating phase (around $t \approx 100$), they fail to reproduce the subsequent sustained workload increase associated with a burst event in the ASU Sol dataset. As a result, these models have limited ability to capture regime transitions and bursty workload dynamics.

In contrast, the calibrated LEL model does not aim for pointwise accuracy. Instead, its trajectories align with the dominant temporal patterns observed across all datasets while capturing burstiness and variability. This behavior stems from the physics-based workload formulation and indicates that the calibrated parameter set represents physically meaningful workload dynamics rather than a purely statistical fit.

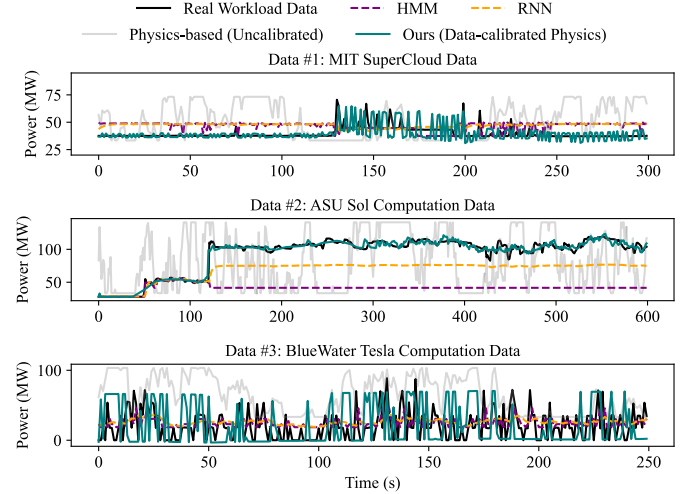


Fig. 4. Comparison between real CPU/GPU workload traces and simulated workload trajectories for three computing sites.

For cooling and auxiliary loads, we use measured cooling-demand profiles and reconstructed auxiliary-load trajectories reported by ASHRAE [36]. The results are shown in Fig. 5 and Fig. 6. The uncalibrated cooling model and default ZIP-based auxiliary model produce smooth or nearly constant responses that fail to capture the abrupt activation and high variability observed in empirical data. Data-driven baselines, such as HMM and RNN, while capable of fitting training data, do not generalize reliably to these subsystems due to the absence of explicit physical structure and are therefore not suitable for reliable transient simulation. After applying the proposed pattern-consistent calibration, the simulated cooling trajectories capture elevated operating regimes and bursty fluctuations characteristic of motor-driven cooling systems, which are not reproduced by data-driven baselines or uncalibrated physics-based models. The calibrated auxiliary load similarly exhibits improved alignment in both amplitude and temporal variation.

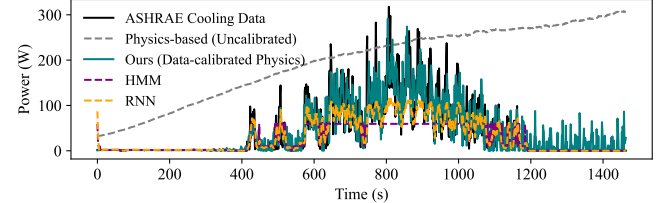


Fig. 5. Empirical cooling load traces and simulated cooling trajectories.

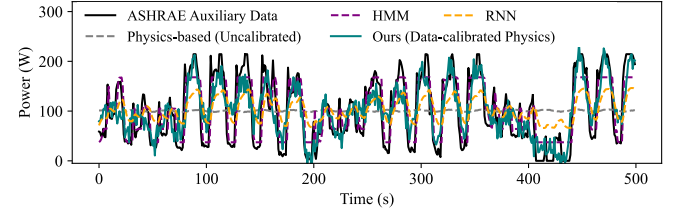


Fig. 6. Empirical auxiliary load traces and simulated auxiliary trajectories.

To quantify similarity between simulated and empirical load trajectories, we use three complementary shape-based metrics: dynamic time warping (DTW) distance, maximum cross-correlation, and cosine similarity. These metrics assess temporal and structural alignment rather than pointwise prediction accuracy, which is not required for system-level

TABLE I

SHAPE SIMILARITY METRICS ACROSS REAL WORKLOAD, COOLING LOAD, AND AUXILIARY LOAD DATASETS. ALL SIMULATED TRACES ARE NORMALIZED PRIOR TO METRIC COMPUTATION.

Metric	Model	MIT Load [34]	ASU Load	BlueWaters Load [35]	Cooling Load [36]	Auxiliary Load [36]
DTW Distance (↓)	HMM	1.407	31.068	4.097	2.943	0.472
	RNN	2.062	14.902	4.878	1.904	0.743
	Physics-based (Uncalibrated)	2.668	17.928	6.568	16.552	1.148
	Ours (Data-calibrated Physics)	1.095	1.278	3.301	1.783	0.308
Max Cross-Corr. (↑)	HMM	-0.067	0.232	0.121	0.775	0.965
	RNN	-0.302	0.962	0.214	0.847	0.961
	Physics-based (Uncalibrated)	-0.179	0.200	-0.011	0.278	0.088
	Ours (Data-calibrated Physics)	0.524	0.981	0.219	0.920	0.970
Cosine Similarity (↑)	HMM	0.994	0.998	0.985	0.996	0.999
	RNN	0.828	0.998	0.580	0.995	0.997
	Physics-based (Uncalibrated)	0.888	0.987	0.649	0.993	0.990
	Ours (Data-calibrated Physics)	0.996	0.999	0.950	0.998	0.999

dynamic analysis. As summarized in Table I, the proposed calibrated physics-based model consistently achieves lower DTW distance and higher cross-correlation and cosine similarity than all baseline models across workload, cooling, and auxiliary datasets. While HMM and RNN baselines perform competitively in isolated metrics or datasets, their performance is less consistent across operating regimes and subsystems.

C. Robustness to Parameter Initialization

Another key to practical deployment of the proposed calibration framework is the robustness to initialization of the parameter set $\{\Theta_{\text{work}}^*, \Theta_{\text{cool}}^*, \Theta_{\text{aux}}^*\}$. Such facility-level parameters are rarely known to utility operators and are typically initialized using industry averages or standard heuristics. We evaluate initialization robustness using the MIT Supercloud dataset by running 20 trials with randomly sampled initial parameters, and compare against an uncalibrated physics-based baseline [18]. As shown in Fig. 7, the baseline model exhibits large dispersion across different initial conditions since it naturally lacks a parameter calibration process. The proposed calibration, on the other hand, shows the ability to converge toward a common, empirically consistent trajectory with significantly reduced variance. This robustness is essential for achieving stable, facility-specific load predictions despite large uncertainty in parameter initialization.

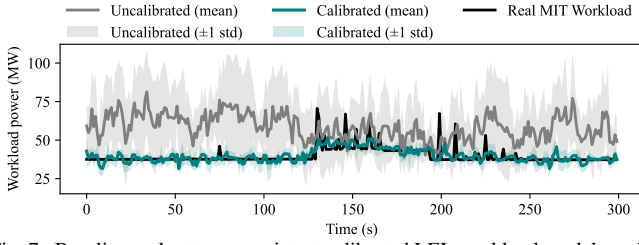


Fig. 7. Baseline and pattern-consistent calibrated LEL workload models under varying parameter initializations.

D. Effect and Sensitivity of the TCL Feature Module

The proposed calibration framework employs TCL to align real and simulated load trajectories in feature space, focusing on temporal patterns and overall magnitude rather than pointwise matching. We evaluate the effectiveness of TCL through a series of ablation and sensitivity studies. Specifically, we

examine: (1) feature representation (TCL versus hand-crafted statistics), (2) calibration loss (feature-wise TCL loss versus sequence-level MSE), (3) representation scope (window-based TCL versus autoencoder), (4) augmentation strategy (full, noise-only, scale-only), (5) temporal window length ($L = 3, 5, 10$), and (6) feature dimension ($d = 16, 64, 256$). In Fig. 8, we report the TCL contrastive loss and the DTW distance between real and calibrated simulated trajectories.

The full TCL with $L = 5$ and $d = 64$ yields the lowest DTW distance among all methods. In contrast, calibration based on pure MSE loss, hand-crafted features, or autoencoder representations results in substantially larger DTW errors, indicating poorer recovery of temporal patterns. Sensitivity results further show that window-based feature extraction is critical: overly short or long windows degrade load alignment. This is probably because data center loads exhibit bursty multi-timescale dynamics that could be underrepresented by overly short windows and oversmoothed by excessively long windows. Meanwhile, extreme feature dimensions provide limited benefit. Overall, these results confirm that TCL offers a compact and effective representation for load calibration, enabling consistent patterns while maintaining robustness across modeling choices.

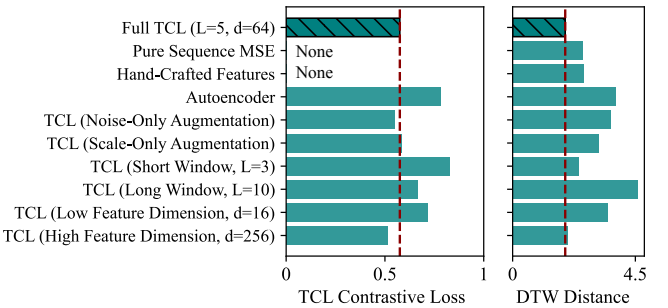


Fig. 8. Ablation and sensitivity analysis of the TCL-based calibration.

E. System-Level Dynamic Response with heterogeneous LEL

After validating the accuracy of the proposed load modeling approach, we integrate the calibrated load models into ANDES [33] to evaluate system-level dynamic responses with heterogeneous LELs connected to the grid. Interactions among heterogeneous LELs can significantly influence grid dynamics,

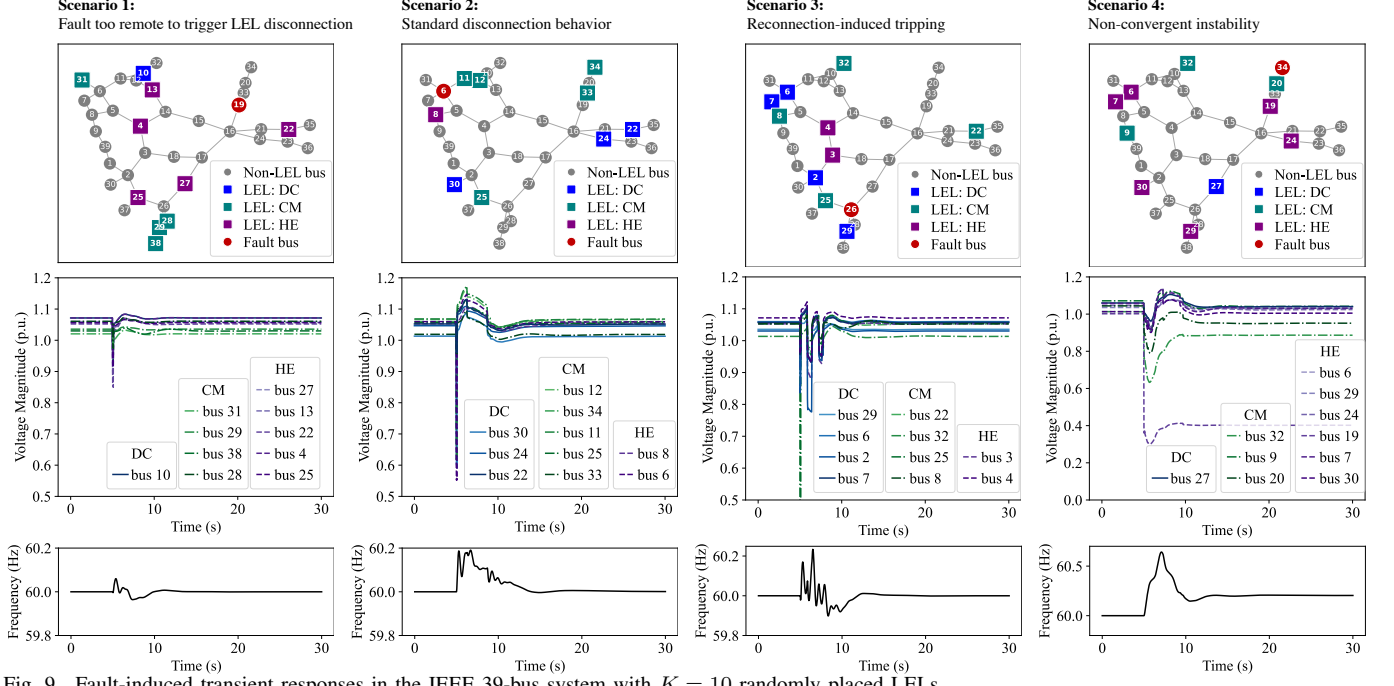


Fig. 9. Fault-induced transient responses in the IEEE 39-bus system with $K = 10$ randomly placed LELs.

yet remain largely underexplored in existing studies. We consider the IEEE 39-bus system and randomly select $K = 10$ buses as LEL sites to reflect their increasing penetration. Each selected bus is randomly assigned to represent a data center, a cryptocurrency mining facility, or a hydrogen electrolyzer. Across these experiments, we observe four qualitatively distinct system response regimes with increasing severity, which are summarized in Fig. 9. In *Scenario 1*, LEL buses are electrically distant from the simulated fault, resulting in only modest voltage sags and allowing all LELs to ride through the disturbance without triggering protection mechanisms. In *Scenario 2*, the voltage sag is deep enough to exceed protection thresholds, resulting in near-simultaneous disconnections of multiple LELs. The sudden loss of load causes the system frequency to rise above nominal and then gradually return after fault clearance. This response closely mirrors utility-reported disturbance events involving LELs [3], [4].

In *Scenario 3*, more critical interaction effects emerge: following the initial disconnection, the reconnection of one data center (bus 29) induces an additional voltage sag for one hydrogen electrolyzer (bus 3), which in turn triggers its protection-driven disconnection. This compound disconnection-reconnection sequence amplifies system stress and increases the risk of cascading failure. In *Scenario 4*, persistent voltage and frequency deviations (with no additional grid recovery actions) prevent one LEL from reconnecting. It indicates the absence of a feasible post-fault operating equilibrium. The sustained loss of load, together with unresolved frequency deviation, ultimately drives the system toward collapse in simulation.

Such a spectrum of transient behaviors is difficult to capture with uncalibrated or homogeneous load representations. The calibrated modeling framework reveals how heterogeneous LELs can fundamentally reshape post-disturbance recovery and amplify localized faults into system-level events.

F. Impact of Load Model Calibration

To examine how different load modeling choices impact transient simulation results, we compare the proposed LEL model with two representative baselines under identical fault scenarios on the IEEE 39-bus system: a conventional ZIP load model and a physics-based LEL model with protection logic [18]. As shown in Fig. 10, the ZIP model fails to trigger load tripping due to the absence of protection mechanisms, rendering it unsuitable for LEL transient analysis. The physics-based baseline captures protection-driven disconnection but yields early load restoration that may underestimate post-fault system stress. This is because, without calibration, both the magnitude and temporal evolution of load shedding are misrepresented. In contrast, the proposed calibrated model yields staged reconnection behavior consistent with reported utility events [3], [4]. It correctly identifies extended recovery intervals and potential constraint violations that are missed by the baseline. These differences indicate that the proposed calibration captures system behavior more realistically, leading to improved operational assessment compared with existing approaches.

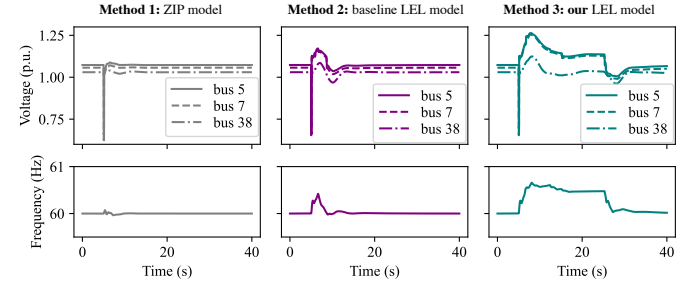


Fig. 10. Comparison of proposed LEL modeling with two baseline load models under identical LEL placement in the IEEE 39-bus system.

To isolate the impact of calibration, we compare the proposed LEL model with and without calibration process. System-level responses are quantified using three metrics: (1)

voltage nadir, defined as the minimum post-fault bus voltage, (2) frequency overshoot, defined as the maximum frequency deviation during recovery, and (3) reconnection delay, defined as the time between fault clearing and successful LEL reconnection, which reflects post-disturbance load restoration difficulty. We perform 20 trials under different LEL placements ($K = 10$) and fault locations, which are kept identical across calibrated and uncalibrated simulations to ensure a fair comparison. As shown in Fig. 11, the calibrated model produces tightly clustered responses across all metrics, whereas the uncalibrated baseline exhibits much larger dispersion. The reduced variability indicates that calibration yields repeatable and statistically stable dynamic responses. This is critical for practical grid studies, where planning, contingency screening, and protection assessment require reliable and interpretable simulation outcomes.

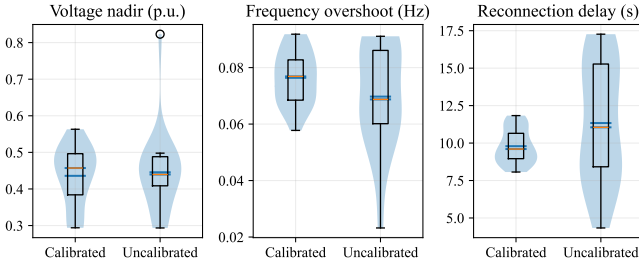


Fig. 11. Comparison between the proposed LEL model with and without the calibration process.

G. Scalability to Large-Scale Power Systems

To evaluate the stability of the proposed model across systems of different scales, we conduct simulations on two larger benchmark systems: the NPCC 140-bus and WECC 179-bus networks. In both cases, the number of LEL sites is fixed to $K = 10$, with locations and types randomly assigned following the same modeling and calibration procedures used for the IEEE 39-bus system.

Simulation results in Fig. 12 confirm that LEL disconnections are consistently reproduced in both large-scale systems, demonstrating that the proposed framework generalizes beyond small test networks. Compared to the IEEE 39-bus case, two systematic differences are observed. First, post-fault voltage and frequency oscillations exhibit reduced peak magnitudes. Second, recovery dynamics are more prolonged in time. These effects are physically consistent with properties of larger interconnected systems. Increased network size and inertia reduce the immediate impact of localized faults on electrically distant buses, leading to smaller instantaneous deviations. However, after LEL disconnections occur, restoring equilibrium requires coordination over a wider area, which leads to slower recovery and longer-lasting oscillations.

H. Sensitivity to LEL Penetration Level

We further examine how increasing LEL penetration influences system dynamics using three system-level metrics: voltage nadir, frequency overshoot, and reconnection delay (see Section IV-F for definitions). Different penetration levels

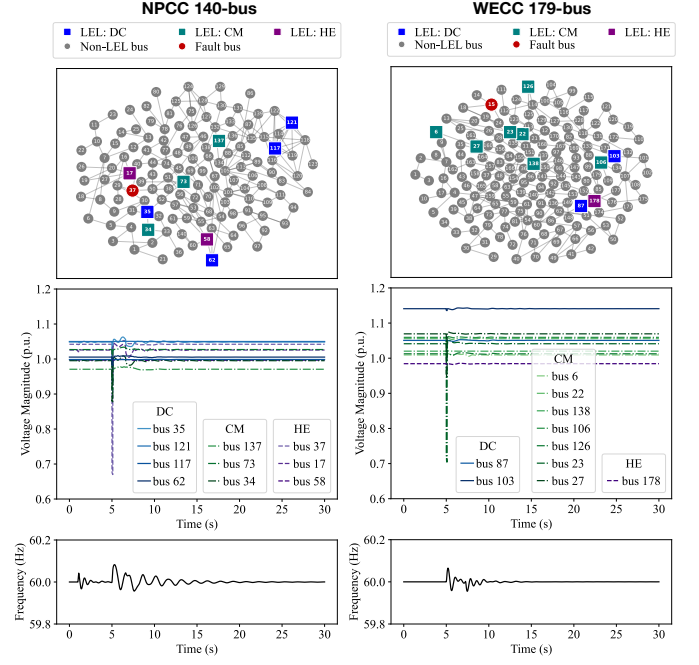


Fig. 12. Fault-induced transient responses in the NPCC 140-bus and WECC 179-bus systems with $K = 10$ randomly placed LELs.

are represented by varying the value of K in the WECC 179-bus system, while keeping all other modeling and disturbance settings fixed. Fig. 13 summarizes the resulting trends.

As LEL penetration increases, all three metrics exhibit systematic degradation: voltage nadirs decrease, frequency overshoots increase, and reconnection delays become longer. These trends indicate that higher LEL presence amplifies both the immediate severity of fault-induced disturbances and the difficulty of system recovery. Notably, the proposed calibrated model reveals smooth and monotonic relationships between penetration level and system response, enabling clear interpretation of how incremental LEL deployment impacts grid dynamics. In contrast, the same LEL model without calibration process produce irregular and inconsistent trends that obscure these relationships. This sensitivity analysis demonstrates that increasing LEL penetration fundamentally alters disturbance and recovery characteristics, and that accurate, calibrated load modeling is essential for reliably assessing these effects in planning and protection studies.

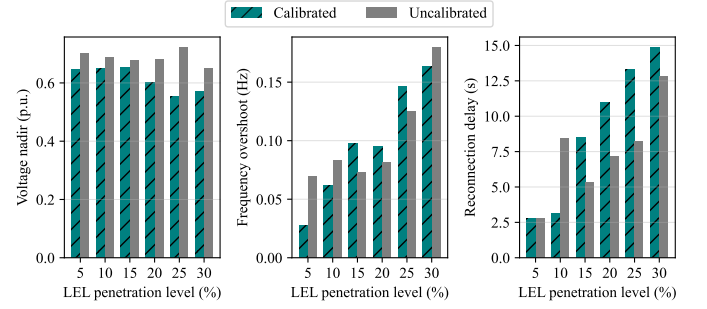


Fig. 13. Sensitivity of voltage, frequency, and recovery dynamics to LEL penetration for calibrated and uncalibrated models.

V. CONCLUSION

This paper proposes a calibrated dynamic load modeling framework for large electronic loads (LELs), such as data centers. It is built on a physics-based backbone capturing

workload variability, cooling and auxiliary dynamics, and protection-driven disconnection and reconnection behavior relevant to grid stability. Building on this structure, we develop a pattern-consistent calibration approach using temporal contrastive learning (TCL) to align model parameters with real operational data through representative temporal patterns rather than exact trajectories. The framework targets realistic, physics-consistent LEL simulation rather than load forecasting, preserves data privacy through local parameter calibration, and supports system-level dynamic studies. Experimental results show that the calibrated model reproduces real-world load behavior, and ANDES-based simulations demonstrate disturbance and recovery responses consistent with utility-reported events across systems of varying scales and LEL penetration levels. Future work will extend this framework toward proactive control strategies for mitigating LEL-induced operational risks.

REFERENCES

- [1] X. Chen, X. Wang, A. Colacelli, M. Lee, and L. Xie, “Electricity demand and grid impacts of AI data centers: Challenges and prospects,” *arXiv preprint arXiv:2509.07218*, 2025.
- [2] North American Electric Reliability Corporation, “LLTF kickoff presentations,” Oct. 2024, accessed: Jan. 2025. [Online]. Available: https://www.nerc.com/globalassets/who-we-are/standing-committees/tc/lltf/lltf_kickoff_presentations.pdf
- [3] Electric Reliability Council of Texas, “NOGRR282: Large electronic load ride-through requirements and NPPR1308,” ERCOT technical and market rule document, Dec. 2025, accessed: Jan. 2026. [Online]. Available: <https://www.ercot.com/files/docs/2025/12/01/6.2-NOGRR282-Large-Electronic-Load-Ride-Through-Requirements-and-NPPR1308.pdf>
- [4] M. Shamseldein, “From liability to asset: A three-mode grid-forming control framework for centralized data center UPS systems,” *arXiv preprint arXiv:2512.16497*, 2025.
- [5] S. Ghosh and M. A. H. Sadi, “Enhancing grid resilience for giga-watt scale data centers using high voltage circuit breaker operated braking resistors,” *arXiv preprint arXiv:2512.21295*, 2025.
- [6] H. Wan, L. Fang, and X. Li, “Grid operational benefit analysis of data center spatial flexibility: Congestion relief, renewable energy curtailment reduction, and cost saving,” *arXiv preprint arXiv:2511.08759*, 2025.
- [7] North American Electric Reliability Corporation, “2025 state of reliability overview,” North American Electric Reliability Corporation, Technical Report, Jun. 2025, accessed: Jan. 2026. [Online]. Available: https://www.nerc.com/globalassets/programs/rapa/pa/nerc_sor_2025_overview.pdf
- [8] Electric Reliability Council of Texas, “Large load stability studies whitepaper,” Electric Reliability Council of Texas, White Paper, 2025, accessed: Jan. 2026. [Online]. Available: https://www.ercot.com/files/documents/2025/08/25/Large_Load_Stability_Whitepaper.pdf
- [9] G. Jang, S. Venkata, and S.-H. Kwon, “An electric arc furnaces load model for transient analysis,” *The Transactions of the Korean Institute of Electrical Engineers*, vol. 48, no. 3, pp. 197–202, 1999.
- [10] G. W. Chang, S.-J. Lin, Y.-Y. Chen, H.-J. Lu, H.-H. Chen, and Y.-R. Chang, “An advanced EAF model for voltage fluctuation propagation study,” *IEEE Transactions on Power Delivery*, vol. 32, no. 2, pp. 980–988, 2017.
- [11] Q. Huang *et al.*, “A generic modeling and development approach for WECC composite load model,” *Electric Power Systems Research*, vol. 172, pp. 1–10, 2019.
- [12] A. Arif, Z. Wang, J. Wang, B. Mather, H. Bashualdo, and D. Zhao, “Load modeling-a review,” *IEEE Transactions on Smart Grid*, vol. 9, no. 6, pp. 5986–5999, 2018.
- [13] V. Logar, D. Dovžan, and I. Škrjanc, “Modeling and validation of an electric arc furnace: Part 1, heat and mass transfer,” *ISIJ international*, vol. 52, no. 3, pp. 402–412, 2012.
- [14] P. Parikh, M. Ali, N. Virani, and S. C. Evans, “Strain to synergy: Powering AI data centers with sustainable and smart power grid infrastructures,” in *IEEE International Conference on Communications, Control, and Computing Technologies for Smart Grids*, 2025, pp. 1–6.
- [15] A. Bajracharya, M. R. A. Khan, S. Michael, and R. Tonkoski, “Forecasting data center load using hidden markov model,” in *North American Power Symposium*, 2018, pp. 1–5.
- [16] M. S. Karabinaoğlu and T. Gözel, “Load profile analysis of data centers and its systems with feature effect comparison,” in *IEEE PES Innovative Smart Grid Technologies Conference Europe*, 2018, pp. 1–6.
- [17] J. Kumar, R. Goomer, and A. K. Singh, “Long short term memory recurrent neural network (LSTM-RNN) based workload forecasting model for cloud datacenters,” *Procedia Computer Science*, vol. 125, pp. 676–682, 2018.
- [18] A. Jimenez-Ruiz and F. Milano, “Data center model for transient stability analysis of power systems,” *arXiv preprint arXiv:2505.16575*, 2025.
- [19] A. Peivandizadeh, “A theoretical framework for virtual power plant integration with gigawatt-scale AI data centers: Multi-timescale control and stability analysis,” *arXiv preprint arXiv:2506.17284*, 2025.
- [20] M.-S. Ko and H. Zhu, “Wide-area power system oscillations from large-scale AI workloads,” *arXiv preprint arXiv:2508.16457*, 2025.
- [21] K.-B. Kwon, S. Mukherjee, and V. Adetola, “Operational risks in grid integration of large data center loads: Characteristics, stability assessments, and sensitivity studies,” *arXiv preprint arXiv:2510.05437*, 2025.
- [22] Y. Xie, W. Cui, and A. Wierman, “Enhancing data center low-voltage ride-through,” *arXiv preprint arXiv:2510.03867*, 2025.
- [23] C. Roberts, E. M. Stewart, and F. Milano, “Validation of the Ornstein-Uhlenbeck process for load modeling based on μ PMU measurements,” in *Power Systems Computation Conference*, 2016, pp. 1–7.
- [24] F. Milano, *Power system modelling and scripting*. Springer Science & Business Media, 2010.
- [25] J. Conto, Y. Cheng, J. Rose, and J. Schmall, “Texas loads ride toward grid stability: Voltage ride through of large power electronic loads,” *IEEE Power and Energy Magazine*, vol. 23, no. 5, pp. 56–67, 2025.
- [26] J. Liu and S. Chen, “Timesurl: Self-supervised contrastive learning for universal time series representation learning,” in *Proceedings of the AAAI conference on artificial intelligence*, vol. 38, no. 12, 2024, pp. 13918–13926.
- [27] A. Menati, K. Lee, and L. Xie, “Modeling and analysis of utilizing cryptocurrency mining for demand flexibility in electric energy systems: A synthetic Texas grid case study,” *IEEE Transactions on Energy Markets, Policy and Regulation*, vol. 1, no. 1, pp. 1–10, 2023.
- [28] G. Ahmad *et al.*, “Load modeling for cryptocurrency mining devices using system identification and machine learning,” in *IEEE International Multi-Conference on Systems, Signals & Devices*, 2025, pp. 516–521.
- [29] M. Tavanaee, M. Cheah-Mañe, O. Gomis-Bellmunt, and E. Prieto-Araujo, “Fault ride-through for hydrogen electrolyzers,” in *IEEE PES Innovative Smart Grid Technologies Conference Europe*, 2025, pp. 1–5.
- [30] A. M. De Corato, M. Ghazavi Dozein, S. Riaz, and P. Mancarella, “Hydrogen electrolyzer load modelling for steady-state power system studies,” *IEEE Transactions on Power Delivery*, vol. 38, no. 6, pp. 4312–4323, 2023.
- [31] I. Goldsmith and Z. Byrum, “Powering the us data center boom: Why forecasting can be so tricky,” 2025, accessed: Jan. 2026. [Online]. Available: <https://www.wri.org/insights/us-data-centers-electricity-demand-and>
- [32] S. Moss, “U.S. DOE cancels plan to survey crypto miners’ electricity use, deletes data,” 2024, accessed: Jan. 2026. [Online]. Available: <https://www.datacenterdynamics.com/en/news/us-doe-cancels-plan-to-survey-crypto-miners-electricity-use-deletes-data/>
- [33] H. Cui, F. Li, and K. Tomsovic, “Hybrid symbolic-numeric framework for power system modeling and analysis,” *IEEE Transactions on Power Systems*, vol. 36, no. 2, pp. 1373–1384, 2020.
- [34] S. Samsi *et al.*, “The MIT supercloud dataset,” in *IEEE High Performance Extreme Computing Conference*, 2021, pp. 1–8.
- [35] Blue Waters Project, “Blue waters system monitoring data set,” 2025, accessed: Jan. 2026. [Online]. Available: <https://bluewaters.ncsa.illinois.edu/data-sets>
- [36] R. American Society of Heating and A.-C. Engineers, “ASHRAE-great energy predictor III,” 2019, accessed: Jan. 2026. [Online]. Available: <https://www.kaggle.com/c/ashrae-energy-prediction>
- [37] M. C. Offutt and L. Zhu, “Data centers and their energy consumption: Frequently asked questions,” Congressional Research Service, Washington, D.C., CRS Report R48646, Aug. 26 2025. [Online]. Available: https://www.congress.gov/crs_external_products/R/PDF/R48646/R48646.1.pdf
- [38] D. Kosterev *et al.*, “Load modeling in power system studies: WECC progress update,” in *IEEE Power and Energy Society General Meeting-Conversion and Delivery of Electrical Energy in the 21st Century*, 2008, pp. 1–8.